Radiation fog properties in two consecutive events under polluted and clean conditions in the Yangtze River Delta, China: A simulation study

Naifu Shao[1], Chunsong Lu[1], Xingcan Jia[2], Yuan Wang[3], Yubin Li[1], Yan Yin[1], Bin Zhu[1], Tianliang Zhao[1], Duanyang Liu[4,5], Shengjie Niu[1,6], Shuxian Fan[1], Shuqi Yan[4,5], Jingjing Lv[1]

[1]Key Laboratory for Aerosol-Cloud-Precipitation of China Meteorological Administration/Collaborative Innovation Centre on Forecast and Evaluation of Meteorological Disasters (CIC-FEMD), Nanjing University of Information Science & Technology, Nanjing, China
[2]Institute of Urban Meteorology, China Meteorological Administration (CMA), Beijing 100089, China
[3]Collaborative Innovation Centre for Western Ecological Safety, Lanzhou University, Lanzhou 730000, China.
[4]Nanjing Joint Institute for Atmospheric Sciences, Nanjing 211112, China
[5]Key Laboratory of Transportation Meteorology, CMA, Nanjing 210009, China
[6]College of Safety Science and Engineering, Nanjing Technology University, Nanjing 210009, China

Correspondence to: Chunsong Lu (luchunsong110@gmail.com)

Abstract. Aerosol–fog interaction (AFI) and planetary boundary layer (PBL) conditions play critical roles in the fog life cycle. However, it is not clear how AFI in the first fog (Fog1) affects PBL and then AFI in the second fog (Fog2), which is important to understand the interaction between AFI and PBL as well as their effects on fog properties. To fill this knowledge gap, our study simulates two successive radiation fog events in the Yangtze River Delta, China, using the Weather Research and Forecasting model coupled with Chemistry (WRF-Chem). Our simulations indicate that conducive PBL conditions are affected by AFI with high aerosol loading in Fog1, and then PBL promotes AFI in Fog2, resulting in higher liquid water content, higher droplet number concentration, smaller droplet size, larger fog optical depth, wider fog distribution, and longer fog lifetime in Fog2 than in Fog1. This phenomenon is related to the following physical factors. The first one is conducive meteorological conditions between the two fog events, including low temperature, high humidity, and high stability. The second one is the feedbacks between microphysics and radiative cooling. A higher fog droplet number

concentration increases the liquid water path and fog optical depth, thereby enhancing the long-wave radiative cooling and condensation near the fog top. The third one is the feedbacks between macrophysics, radiation, and turbulence. A higher fog top presents stronger long-wave radiative cooling near the fog top than near the fog base, which weakens temperature inversion and strengthens turbulence, ultimately increasing the fog-top height and fog area.

In summary, AFI postpones the dissipation of Fog1 due to these two feedbacks and generates more conducive PBL meteorological conditions before Fog2 than before Fog1. These more conducive conditions promote the earlier formation of Fog2, further enhancing the two feedbacks and strengthening the AFI. Our findings are critical for studying the interaction between aerosol, fog, and PBL, but also shed new light on aerosol–cloud interaction.

1 Introduction

Fog comprises many water droplets or ice crystals suspended above the ground (WMO, 1992). This leads to low visibility, affecting the human health, transportation, and power system (Niu et al., 2010). There exist uncertainties in fog forecasting (Zhou and Du, 2010; Zhou et al., 2011). An important reason is that the physical processes of fog remain unclear, because many processes (aerosol activation, condensation, radiation as well as turbulence) not only occur simultaneously but also interact with each other nonlinearly (Haeffelin et al., 2010), which affects fog properties (Mazoyer et al., 2022) and impedes the related parameterisation (Poku et al., 2021). To better understand the physical processes of fog, comprehensive studies have been conducted based on observations and simulations (Fernando et al., 2021; Gultepe et al., 2014; Guo et al., 2015; Hammer et al., 2014; Liu et al., 2011; Price et al., 2018; Shen et al., 2018; Wang et al., 2021). The critical roles of aerosols and the planetary boundary layer (PBL) in these processes have been shown (Boutle et al., 2018; Niu et al., 2011; Quan et al., 2021).

Aerosol–fog interaction (AFI) reflects the response of fog properties to changes in aerosol loading. Since fog is a special type of cloud (Guo et al., 2021; Kim and Yum, 2010, 2013; Wang et al., 2023), AFI is expected to share similarities with aerosol–cloud interaction. Studies on aerosol–cloud interaction revealed that increasing aerosol loading increased cloud droplet concentration, thereby increasing the cloud optical depth under a constant liquid water content (LWC) (Garrett and Zhao, 2006; Twomey, 1977; Wang et al., 2013; Wang et al., 2018; Zhao and Garrett, 2015). Different continental fog observation projects showed that fog microphysical properties were significantly affected by aerosol loading (Mazoyer et al., 2019; Niu et al., 2011; Quan et al., 2011; Wang et al., 2021). In those polluted fog observations, for instance, Quan et al. (2011) found that the fog droplet number concentration (N_f) was higher than 1,000 cm^{-3} and effective radius (R_e) was approximately 7 μm in the North China Plain. In those clean fog observations, for example, Wang et al. (2021) showed that N_f was smaller than 100 cm^{-3} and R_e was approximately 9 μm in the tropical rainforest in Xishuangbanna, China. Several simulation studies reproduced these observations, and demonstrated the complex impacts of AFI on fog micro- and macrophysics (Jia et al., 2019; Maalick et al., 2016; Stolaki et al., 2015; Yan et al., 2020). Regarding fog microphysics, increasing aerosol loading increased N_f and LWC due to increased activation and condensation in simulations (Jia et al., 2019; Stolaki et al., 2015; Yan et al., 2020). Regarding fog macrophysics, some model studies revealed that increased aerosol loading increased the fog-top height (Jia et al., 2019; Stolaki et al., 2015) and prolonged the fog lifetime by delaying its dissipation (Quan et al., 2021; Yan et al., 2021).

Furthermore, previous studies found that meteorological conditions played crucial roles in aerosol–cloud interaction as well as cloud macro- and microphysics (Ackerman et al., 2004; Kumar et al., 2017; Kumar et al., 2021; Liu et al., 2019; Liu et al., 2020; Toll et al., 2019). Similarly, studies on fog showed that AFI was affected by meteorological conditions in the PBL (e.g., radiation, thermodynamics, and dynamics), which further affected fog micro- and macrophysics (Haeffelin et al., 2010). Early studies showed that radiative cooling was an important factor for temperature inversion, providing stable conditions for fog formation (Fitzjarrald and Lala, 1989; Holets and Swanson, 1981; Roach et al., 1976). According to Zhou and Ferrier (2008), turbulence may suppress or deepen the fog-top height, which was related to the critical turbulence coefficient. The critical turbulence coefficient was the turbulence threshold for diagnosing whether turbulence suppressed fog or not. If the turbulence intensity inside fog was weaker than the critical turbulence coefficient, the fog persisted; otherwise, the fog dissipated (Zhou and Ferrier, 2008). If temperature inversion was weak, excessive vertical turbulent mixing delayed fog formation (Maronga and Bosveld, 2017). However, if temperature inversion was sufficiently strong, vertical turbulent mixing at the middle and fog base increased the fog top height, as proposed based on observations (Ye et al., 2015) and simulations (Porson et al., 2011). Consequently, turbulence may affect fog macrophysics. Furthermore, aerosols affect turbulence, thereby impacting fog macrophysics (Jia et al., 2019; Quan et al., 2021). A previous qualitative analysis revealed that aerosols promoted turbulence and horizontal distribution because of weaker temperature inversion (Jia et al., 2019).

Previous studies typically focused on an individual fog event or analysed multiple fog events statistically, however, there were still several studies mentioning that LWC, N_f, and liquid water path (LWP) in the latter fog scenario were larger than those in the preceding one (Quan et al., 2011; Wærsted et al., 2017). What are the physical mechanisms behind the property changes during the two successive fog events? Furthermore, which fog scenario has fog macro- and microphysical properties that are more sensitive to aerosol loading, i.e., experiencing stronger AFI? Are the mechanisms related to the interaction between AFI and PBL? To answer these questions, two successive radiation fog events in the Yangtze River Delta (YRD) region in China are simulated in this article using the Weather Research and

Forecasting model coupled with Chemistry (WRF-Chem). The two fog scenarios provide an excellent opportunity to analyse AFI under polluted conditions as a chain, i.e., how high aerosol loading affects properties in the first fog scenario, how the properties in the first polluted fog scenario affect radiation and the PBL structure, and then how radiation and the PBL affect properties and AFI in the second fog scenario under polluted conditions. Additionally, because fog is a special cloud near ground, the evolution of AFI is also helpful to study the evolution of aerosol–cloud interaction, which is critical to climate prediction (Boutle et al., 2018; Vautard et al., 2009) .

The rest of the article is organized as follows. Section 2 presents descriptions of the two successive fog events, experimental design, and data source. Section 3 presents simulation verification. Section 4 shows larger aerosol-induced changes in Fog2 than in Fog1. Section 5 presents the physical mechanisms underlying the larger aerosol-induced changes in Fog2 than in Fog1. Section 6 summarises the conclusions.

2 Experimental design and data source

Here, we study how radiation fog properties are affected by high aerosol loading and PBL meteorological conditions in two successive events in the YRD region. The $PM_{2.5}$ mass concentration was over 100 μg m^{-3} before fog events in the YRD due to anthropogenic emissions (Zhu et al., 2019). On 26–27 November 2018, two successive radiation fog events occurred in northern YRD. The first fog event is called Fog1, and the second one is called Fog2. Ground-based observations at the Nanjing site (32.2°N 118.7°E) show that the two fog events (visibility <1,000 m) occurred with high relative humidity, low temperature, and weak wind speed (Fig. 1). As shown in Fig. S1, the surface is controlled by a high–pressure system with cold and moist air in the northern YRD at 20:00 local standard time (LST) (LST = Universal Time Coordinated + 8 h) on 26 and 27 November 2018. WRF-Chem (version 4.1.3) is employed to simulate the two successive radiation fog events. WRF-Chem couples physical and chemical processes; therefore, it has been widely utilized to study AFI (Jia et al., 2019; Lee et al., 2016; Yan et al., 2020; Yan et al., 2021). The model is integrated from 14:00 LST on 24 November 2018 to 14:00 LST on 27 November 2018, with the first 24 hours regarded as the spin-up time. As shown in Fig. S2, the model is configured using three nested domains, and the domain centres are all located in Nanjing. The three nested domains are 90 × 122, 118 × 142, and 130 × 154 grid cells with resolutions of 27, 9, and 3 km, respectively. The simulation area covers the major weather system, which can affect the YRD. There are 36 vertical levels in the model, of which 17 layers are located in the lowest 500 m above the ground. Moreover, Yang et al. (2019) noted better fog simulation performance when the bottom layer was 8 m above the ground because this layer affected the interaction between fog and surface flux. Consequently, we set the model bottom layer as 8 m in the present study. In addition, the model is driven by the National Centre for Environmental Prediction (NCEP) Final (FNL) 1°×1° reanalysis data (https://rda.ucar.edu/datasets/ds083.2/) (Ding et al., 2019; Jia et al., 2019). The Multiresolution Emission Inventory for China (MEIC) database (http://meicmodel.org) is used for anthropogenic emissions in the model (Li et al., 2017a; Zheng et al., 2018).

Table 1 shows the parameterisation schemes of physical processes used in the present study. The microphysics scheme is Morrison (Morrison et al., 2005) coupled with the activation scheme (Abdul-Razzak, 2002). The PBL scheme is MYNN2.5 (Nakanishi and Niino, 2009). Turbulence is parameterised in the MYNN2.5 scheme and there is also a sub-grid cloud parameterisation (Chaboureau and Bechtold, 2002) in the MYNN2.5 scheme. The radiation schemes are coupled with the aerosol–cloud–radiation interaction. The long- and short-wave radiation schemes are RRTMG (Iacono et al., 2008) and Goddard (Matsui et al., 2020), respectively. The cumulus scheme is Grell 3D (Grell and Dévényi, 2002). The chemistry schemes are MOSAIC-4 bins (Zaveri et al., 2008) and CBMZ (Zaveri and Peters, 1999).

For model verification, meteorological data are retrieved from the China Meteorological Administration (http://www.nmic.cn/), satellite data are retrieved from the Himawari-8 geostationary satellite (https://www. eorc.jaxa.jp/ptree/index.html), and $PM_{2.5}$ mass concentration data are from the Ministry of Environmental Protection (https://quotsoft.net/air/).

To investigate the aerosol-induced changes in the fog macro- and microphysics, one control run and two sensitivity tests are conducted, which are called EXP1, EXP2, and EXP3, respectively. High and low emissions are used to represent polluted and clean conditions, respectively. Their difference can indicate the aerosol effect on fog properties. In the EXP1, the emission intensity is taken directly from the MEIC database to simulate fog under polluted conditions. In the EXP2, the emission intensity is multiplied by 0.05 to simulate fog under clean conditions, as described in studies by Jia et al. (2019) and Yan et al. (2021). In the EXP3, Fog1 is under the clean condition (5% of emission from the MEIC database) and Fog2 is under the polluted condition (the default emission from the MEIC database). Particularly, according to Fog1 dissipate time, the clean condition is set before 11:00 LST on 26 November 2018, and the polluted condition is set after 12:00 LST on 26 November 2018. Compared with the difference between the EXP1 and EXP2, the difference between the EXP3 and EXP2 reveals whether the fog properties and AFI with higher aerosol loading in Fog1 can affect those in Fog2 or not.

3 Simulation verification

Simulation verifications for temperature, relative humidity, and wind speed are shown in Fig. 2. The correlation coefficients of 2 m temperature (T_{2m}), 2 m relative humidity (RH_{2m}), and 10 m wind speed (WS_{10m}) between the simulations and observations are 0.9, 0.9, and 0.6, respectively, passing the significance test at 99%. Therefore, the simulations are generally consistent with the observations. The mean deviations of T_{2m}, RH_{2m}, and WS_{10m} between the simulations and observations are 1.0 °C, 2.7%, and 0.4 m s^{-1}, respectively, consistent with evaluation results in studies by Hu et al. (2021), Gao et al. (2016), and Yang et al. (2022). Figure 3 shows the evaluation of $PM_{2.5}$ distribution, and Table 2 summarises statistics of the mean mass concentration of $PM_{2.5}$ based on the method proposed by Boylan and Russell (2006). The normalised mean bias (NMB), normalised mean error (NME), mean fractional bias (MFB), and mean fractional error (MFE) between the simulations and observations are 25%, 30%, 24%, and 28%, respectively (Eqs. S1-S4). Although the $PM_{2.5}$ mass concentration is overestimated, it remains within a reasonable range (Shu et al., 2021; Yang et al., 2022; Zhai et al., 2018).

Figure 4 shows the evaluation of fog spatial distribution. The simulated fog optical depth (FOD) distribution is compared with the Himawari-8 cloud optical depth products and ground-based observations (the black circles in Fig. 4) at 08:00 LST on 26 and 27 November 2018, respectively. Qualitatively, the simulated fog spatial distribution and magnitude are generally consistent with satellite and ground-based observations. Similarly, Lee et al. (2016) evaluated fog distribution simulation against cloud optical depth from satellite; they also concluded that the distributions of simulation and observation were generally comparable with each other.

To further quantitatively evaluate the simulation, the Heidke skill score (HSS) is calculated (Barnston, 1992):

$$HSS = \frac{2(ad - bc)}{(a+c)(c+d)+(a+b)(b+d)} \quad (1)$$

Elements *a*–*d* are the numbers of "hits", "false alarms", "misses", and "correct negatives", respectively, which are determined by observations and simulations as shown in Table 3. To identify observed fog at a station, two criteria are used: visibility less than 1 km and relative humidity larger than 90% (Yan et al., 2020). Simulated foggy grids are recognized based on three criteria (Jia et al., 2019; Zhao et al., 2013): fog water mixing ratio over 0.01 g kg^{-1}, N_f greater than 1 cm^{-3}, and fog base touching the ground. The elements *a*–*d* are calculated based on the fog occurrence at the observation stations and the closest model grids. The perfect HSS score is 1.0, indicating that simulations are identical to observations. Here, the HSS score are 0.34 and 0.36 in Fog1 and Fog2, respectively, which are close to previous reports (Mecikalski et al., 2008; Xu et al., 2020; Yamane et al., 2010). Therefore, the model can generally capture the fog spatial distribution.

4 Larger aerosol-induced changes in Fog2 than in Fog1

Here, we analyse the fog macro- and microphysical characteristics under the clean and polluted conditions (Fig. 5). To ensure sufficient sample size for statistical analysis, only data with the fog area fraction larger than 5% are analysed. The fog area fraction is calculated as the number of foggy grid cells divided by the total number of grids in domain 03. We also test other thresholds, 1%, 2.5%, 7.5%, and 10% (Fig. S3). The results are similar to those based on the threshold of 5%.

The ratios of changes between the polluted and clean conditions reveal that high aerosol loading affects fog macro- and microphysical properties in Fog1 and Fog2 (Fig. 5a). Compared to fog microphysics under clean conditions, N_f and LWC in Fog1 increase by respectively 463.0% and 81.7%, but R_e decreased to 32.1% under polluted conditions. Furthermore, because of the AFI, N_f and LWC in Fog2 increase by respectively 672.4% and 113.5%, but R_e decreases by 40.0%. Therefore, aerosol-induced changes in Fog2 are larger than those in Fog1, as shown in Fig. 5a (N_f: 209.5%, LWC: 31.8%, and R_e: -6.9%). Similarly, aerosol-induced changes in fog macrophysics are larger in Fog2. Compared with values under clean conditions, the fog area, fog-top height, and duration in Fog1 increase by respectively 23.1%, 109.6%, and 20.0% under polluted conditions; the corresponding values in Fog2 are larger (34.9%, 350.5%, and 25.0%, respectively). In addition, LWP and FOD show similar trends. With the similar trend between observation and simulation, Figure S4 shows that aerosol mass concentration is similar before

Fog1 and Fog2 formation, and aerosol number concentration before Fog2 is less than that before Fog1 formation. Therefore, changes in aerosol concentration are not the main reason for increasing aerosol-induced changes in the two fog properties. To ensure whether AFI under the polluted condition can lead to this increment of aerosol-induced changes in Fog1 and Fog2, we design a sensitivity test called EXP3, as mentioned above. Furthermore, to quantitatively evaluate the strength of AFI in the two fog events, we examine the responses of FOD to changes in N_f (Eq. 2) (Ghan et al., 2016):

$$\frac{\Delta \ln FOD}{\Delta \ln N_f} = \frac{\Delta \ln LWP}{\Delta \ln N_f} - \frac{\Delta \ln R_e}{\Delta \ln N_f} \tag{2}$$

Based on the similar aerosol concentration background (Fig. S4), the responses of FOD to changes in N_f quantitatively confirm which fog has more remarkable AFI. As shown in Table 4, the strength of AFI in Fog2 (1.32) is larger than that in Fog1 (0.98). If Fog1 is under the clean condition and Fog2 is under the polluted condition (EXP3), AFI in Fog2 is 1.17, which is lower than that in the EXP1 (1.32). It means that high aerosol loading in Fog1 enhances AFI in Fog2. Relative changes in the above properties between Fog1 and Fog2 are calculated as (Fog2 − Fog1)/Fog1. The values of $\Delta\ln FOD/\Delta\ln N_f$, $\Delta\ln LWP/\Delta\ln N_f$, as well as $-\Delta\ln R_e/\Delta\ln N_f$ are 34.7%, 42.1%, and 9.1% larger in Fog2 than in Fog1, respectively. These numbers quantitatively confirm stronger AFI in Fog2 and indicate that LWP is the dominant factor for enhancing AFI. LWP depends on the fog-top height and LWC. As shown in Fig. 5a, when aerosol loading changes from clean to pollution, the rate of increase in fog-top height in Fog2 (350.5%) is much larger than that in Fog1 (109.6%). Although the increase of LWC in Fog2 (113.5%) is also larger than that in Fog1 (81.7%), the magnitude of increase in LWC is smaller than that increase in fog-top height, indicating that AFI are more sensitive to fog-top height than to LWC.

Fog duration is determined by the time of fog formation and dissipation, which is primarily extended because high aerosol loading delays fog dissipation, as reported previously (Jia et al., 2019; Quan et al., 2021). In this article, high aerosol loading not only postpones fog dissipation but also promotes earlier fog formation, particularly during Fog2 (Fig. 5b). Fog formation is related with PBL conditions which can be affected by AFI. To investigate the aerosol effect on the Fog2 formation stage, fog spatial distribution at the formation stage from 19:00 LST to 21:00 LST on 26 November is examined, as shown in Figure 6. The fog area is rather small at 19:00 LST under both polluted and clean conditions. At 20:00 LST, in grid cells located outside the black box, fog formation is similar under both polluted and clean conditions. Inside the black box, there are several foggy grid cells under polluted conditions. At 21:00 LST, fog area in the black box further expands under polluted conditions. However, there is almost no fog in the black box at 20:00 LST and 21:00 LST under clean conditions. Therefore, high aerosol loading promotes earlier formation of Fog2, which is primarily caused by meteorological conditions in the PBL inside the black box. In addition, the fog area outside the black box is larger under polluted conditions than under clean conditions, which is mainly related to the stronger turbulence diffusion under polluted conditions. Detailed analysis is described in Sect. 5.

5 Physical mechanisms underlying the larger aerosol-induced changes in Fog2 than in Fog1

5.1. More conducive meteorological conditions before Fog2

Meteorological conditions in the PBL affect the fog formation time and AFI during fog events. As shown in Table 5, under clean conditions, RH_{2m} before Fog2 formation is higher and PBL height (PBLH) is lower than those before Fog1 formation in domain 03. The polluted conditions have similar results. Furthermore, compared with the difference of aerosol-induced changes in RH_{2m} and PBLH before fog formation, RH_{2m} increases by 6% and PBLH decreases by 92 m under polluted conditions, which is larger than those (RH_{2m}: 4% and PBLH: -59 m) under clean conditions. Therefore, high aerosol loading generates more conducive meteorological conditions for Fog2 formation during two successive fog events.

To further analyse how high aerosol loading promotes Fog2 formation, we focus on the black box in Fig. 6, as described in Sect. 4 and by Yan et al. (2021). The regional average differences in the total optical depth (TOD), downwelling short-wave radiation (SW) at the ground, T_{2m}, PBLH, RH_{2m}, and water vapour mixing ratio (Qv_{bot}) at the model bottom layer (8 m) in the black box between polluted and clean conditions are calculated (Fig. 7). During the daytime before Fog2 formation, meteorological conditions in the PBL are affected by FOD at the Fog1 dissipation stage. Larger TOD, particularly larger FOD, leads to lower SW, T_{2m}, and PBLH. Notably, Qv_{bot} under polluted conditions is lower than that under clean conditions before complete dissipation of Fog1, because of less fog water evaporation. When the fog dissipates completely, the lower PBLH accumulates more water vapour, increasing Qv_{bot} and RH_{2m}. The positive feedbacks between AFI and PBL are similar to the feedbacks between high aerosol loading and PBL reviewed by Li et al. (2017b). Further, the feedback mechanism between high aerosol loading and PBL introduced by Zhong et al. (2018) supports the daytime feedbacks between fog and PBL in the present study. Additionally, aerosol extinction is also considered in TOD. Whether AOD affects PBL significantly or not should also be discussed. As shown in Table 5, RH_{2m} and PBLH before Fog1 on 25 November under clean conditions are 76 % and 669 m, respectively, quite similar to those under polluted conditions (76 % and 670 m, respectively). Therefore, it is not likely that aerosol-meteorology interaction can lead to the meteorological differences in Figure 7. Besides, a previous study (Yan et al., 2021) also noted that aerosol–fog interaction was more remarkable than aerosol–radiation interaction. Therefore, lower temperature, higher relative humidity, and higher stability result from AFI in Fog1, contributing to the earlier formation of Fog2.

Larger FOD and delaying dissipation result in lower temperature, higher relative humidity, and higher stability by affecting solar radiation during the daytime. How can these conducive conditions be maintained after the sunset around 17:00 LST? Figure 8a shows that cold advection is the major reason responsible for the difference in temperature between polluted and clean conditions. We further seek to unveil the reason cold advection is stronger under polluted conditions. Figure 8b shows a cold centre, with wind diverging outward from it. The cold centre is related to lower temperature under polluted conditions due to larger FOD and longer duration in Fog1. Likewise, Steeneveld and De Bode (2018) pointed out that fog appeared earlier with cold advection. In addition, lower PBLH induced by high aerosol loading promote the maintenance of higher humidity and higher stability.

Overall, as mentioned above, the more conducive meteorological conditions promote Fog2 formation due to AFI at the Fog1 dissipation stage. Furthermore, this interaction enhances the feedbacks in the fog physical processes, thus rendering stronger AFI in Fog2. Details are discussed in Sect. 5.2 and 5.3.

5.2. Feedbacks between microphysics and long-wave cooling

Section 5.1 reveals the mechanism through which AFI in Fog1 leads to more conducive meteorological conditions before Fog2 formation. In Sect. 5.2, we demonstrate how conducive meteorological conditions play fundamental roles in promoting the feedbacks between microphysics and long-wave cooling, resulting in stronger AFI in Fog2.

As shown in Fig. 5a, aerosol-induced changes in LWC and N_f during Fog2 are larger than those during Fog1 because lower temperature and higher humidity are more conducive for aerosol activation and fog condensation (Petters and Kreidenweis, 2007; Simmel and Wurzler, 2006). Due to competition for available water vapour (Mazoyer et al., 2022; Yum and Hudson, 2005), R_e in Fog2 is smaller than that in Fog1. Consequently, FOD in Fog2 is larger than that in Fog1. Additionally, increased FOD in Fog2 triggers stronger positive feedbacks between microphysics and long-wave cooling, further enhancing cooling, activation, and condensation and thereby increasing N_f and LWC. Jia et al. (2019) emphasised that high aerosol loading promoted these positive feedbacks. The present study further highlights the synergistic effects of high aerosol loading and meteorological conditions on the enhancement of positive feedbacks, which promote AFI in Fog2.

To better understand how the above positive feedbacks affect AFI, Fig. 9 presents the average extinction coefficient through the fog, that is, FOD at per unit height (FOD/Δh), radiative cooling rate (T_{LW}), condensational growth rate (LWC_{COND}), and LWC tendency due to vertical mixing (LWC_{mixing}) in the two successive fog events. Radiative cooling is the strongest near the fog top and weakest at the fog base (Ducongé et al., 2020; Mazoyer et al., 2017; Wærsted et al., 2017). Consequently, LWC_{COND} and LWC_{mixing} both follow similar profiles in response to radiative cooling. Therefore, if the vertical profiles of the three terms use absolute height, they will be distorted. To overcome this problem, physical quantities are normalised by the fog-top height. Compared with those in Fog1, larger extinction coefficient (Fig. 9a-b), stronger long-wave radiative cooling (Fig. 9c-d), and more condensation (Fig. 9e-f) near the fog top are noted in Fog2 due to conducive PBL conditions before formation, which further increases LWC and fog-top height in Fog2 (the black and purple lines). Enhancement of these parameters indicate that the feedbacks between microphysics and long-wave cooling are stronger in Fog2 than in Fog1. As a result, AFI is stronger in Fog2 than in Fog1, due to favourable PBL conditions caused by AFI in Fog 1. In addition, as shown in Fig. 9g-h, vertical mixing transports fog water from the fog top to the fog base, and the strength of this transportation is stronger in Fog2 than in Fog1, because of stronger turbulent kinetic energy (TKE) in Fog2. The effect of TKE on fog is analysed in Sect. 5.3.

5.3. Feedbacks between macrophysics, radiation, and turbulence

Section 5.2 analyses the microphysics-related mechanisms behind stronger AFI in Fog2. This subsection not only focuses on macrophysics and its feedbacks with radiation and turbulence but also discusses how the combined effects of high aerosol loading and meteorological conditions impact the feedbacks and enhance AFI in Fog2, compared with those in Fog1. Briefly, fog macrophysics involves duration and distribution. The reason why the duration of Fog2 is longer than that of Fog1 is due to the earlier formation of Fog2, which is induced by the more conducive meteorological conditions, as discussed in Sect. 5.1. The reason for the wider distribution (fog-top height and fog area) is discussed here.

5.3.1 Effects of macrophysics on radiation

The more conducive meteorological conditions and AFI promote condensation near the fog top (Fig. 9d, f), thereby raising the fog-top height in Fog2 compared with that in Fog1 (black and purple lines in Fig. 9). Therefore, both fog-top height and FOD in Fog2 are higher than those in Fog1. Compared with that in Fog1, the higher FOD in Fog2 can enhance cooling near the fog top and downwelling long-wave radiation, weakening the cooling at the fog base than near the fog top (Fig. 9c). Additionally, the horizontal distribution of Fog2 is wider than that in Fog1 (Fig. 5b). Therefore, more foggy grid cells show more radiative cooling near the fog top and downwelling long-wave radiation at the fog base in Fog2.

5.3.2 Effects of radiation on turbulence

The above analysis reveals the mechanism of the effects of meteorology and AFI on radiation in fog. How does radiation affect stability and turbulence (i.e., TKE)? To answer this question, we must know the dominant factors contributing to TKE, as described in the following TKE budget equation:

$$\frac{\Delta TKE}{\Delta t} = TKE_{\text{shear}} + TKE_{\text{buoy}} - TKE_{\text{diss}} + TKE_{\text{mixing}} \quad (3)$$

where $\Delta TKE/\Delta t$ is the TKE tendency with time (Fig. 10b), and the four terms on the right side of Eq. (3) are contributors to TKE, including wind shear (Fig. 10c), buoyancy (Fig. 10d), dissipation (Fig. 10e), and vertical mixing (Fig. 10f). Detailed equations of these contributions to TKE are provided in supplementary information (Eqs. S5-S8) (Nakanishi and Niino (2009)).

As shown in Fig. 10a, TKE in Fog2 is stronger than that in Fog1, particularly under polluted conditions. As the vertical mixing term is one order smaller than the others, it is negligible (Fig. 10f). At night, only the shear term is positive and, therefore, the main contributor to TKE (Fig. 10c), consistent with the speculations of Kim and Yum (2012). However, the dominant term driving the differences in TKE between polluted and clean conditions is buoyancy (Fig. 10d). As shown in Fig. 10b, $\Delta TKE/\Delta t$ is larger under polluted conditions than under clean conditions. Meanwhile, the shear term is smaller but the buoyancy term is larger under polluted conditions than under clean conditions; moreover, the dissipation term is similar between the two conditions. Therefore, the buoyancy term is the main factor increasing TKE under polluted conditions, corroborating the qualitative speculations by Jia et al. (2019). This is particularly true for Fog2. In addition, at daytime, $\Delta TKE/\Delta t$ is weaker under polluted conditions, because higher FOD reduces short-wave radiation reaching the surface. These results are consistent with the higher stability during the dissipation stage under polluted conditions, as described in Sect. 5.1.

After confirming the importance of the buoyancy term, we analyse the effect of radiation on buoyancy and then on TKE. Buoyancy contributions to TKE are determined by temperature inversion in the PBL at night time. As shown in Fig. 11a-b, temperature inversion is close to the surface. With the effect of AFI, much stronger radiative cooling leads to a more rapid temperature drop at the fog top than at the fog base (Fig. 11c), thereby causing weaker temperature inversion under polluted conditions. Therefore, stability is weaker and TKE is larger under polluted conditions, particularly in Fog2.

5.3.3 Effects of turbulence on macrophysics

Previous observations (Liu et al., 2010; Román-Cascón et al., 2016) and large eddy simulations (Bergot, 2013; Mazoyer et al., 2017; Nakanishi, 2000) showed that turbulence could increase the fog-top height. In this article, we note that increasing TKE increases fog-top height (black and purple lines in Fig. 9) and fog area (Fig. 5b), which is consistent with observations of Jia et al. (2019) and Quan et al. (2021). The increased fog-top height increases TKE by promoting radiative cooling near the fog top and weakening temperature inversion. This reflects the feedbacks between macrophysics, radiation, and turbulence. Overall, due to the more conducive meteorological conditions, the feedbacks are stronger in Fog2 than in Fog1.

6 Conclusion

To explore the interactions between PBL and AFI as well as their effects on fog properties, WRF-Chem 4.1.3 is used to simulate two successive radiation fog events, which occurs in the northern YRD region in China on 26 and 27 November 2018. The two fog events simulation (Fog1 and Fog2) can well reproduce the observed results.

The results show higher LWC, higher N_f, smaller R_e, higher fog-top height, longer duration, wider spatial distribution, higher LWP, and higher FOD under polluted conditions than under clean conditions. Aerosol-induced changes in micro and macro-physical properties are more significant in Fog2 than in Fog1. If Fog1 is under clean conditions, the response of Fog2 to high aerosol loading becomes weaker. Therefore, AFI with high aerosol loading in Fog1 promotes aerosol-induced changes in Fog2. A conceptual diagram is proposed to describe the mechanism of fog property changes as well as AFI evolution during two successive radiation fog events (Fig. 12). Moreover, the mechanisms of AFI evolution are discussed based on the synergistic effects of aerosols and meteorological conditions. In Fog1, the microphysics–radiation feedbacks and macrophysics–radiation–turbulence feedbacks delay Fog1 dissipation, generating more conducive PBL meteorological conditions and promoting the earlier formation of Fog2. Furthermore, the microphysics–radiation feedbacks and macrophysics–radiation–turbulence feedbacks are strengthened in Fog2 due to more conducive conditions, enhancing AFI in Fog2 compared with those in Fog1. Detailed mechanisms are summarised below, including meteorological conditions and the two types of feedbacks.

First, meteorological conditions before Fog2 formation are more conducive than those before Fog1 formation, which play fundamental roles in changing fog properties and enhancing AFI during two fog events. This is related to the delayed dissipation of Fog1 induced by FOD. During Fog1 dissipation (daytime), the cooling effect caused by the higher FOD contributes to the lower temperature, higher relative humidity, and higher stability. At night, cold advection near the ground is enhanced. Meanwhile, affected by the daytime temperature, the temperature remains low, forming a cold centre. Moreover, the surface wind diverges from the cold centre to the outside, strengthening the cold advection. Ultimately, more conducive meteorological conditions induced by high aerosol loading promote the earlier formation and longer duration of Fog2 than of Fog1.

Second, the positive feedbacks between microphysics and radiative cooling are crucial physical mechanisms for changing fog properties and enhancing AFI. In Fog2, high aerosol loading and more conducive meteorological conditions synergistically promote fog microphysics. Lower temperature and higher relative humidity promote aerosol activation and condensation. Consequently, N_f, LWP, and FOD are higher, whereas R_e is smaller, in Fog2 than in Fog1. These variations in microphysics lead to stronger long-wave radiative cooling and condensational growth near the top of Fog2. Therefore, the positive feedbacks between microphysics and radiation are stronger in Fog2, which further promote stronger AFI.

Finally, the feedbacks between fog macrophysics, radiation, and turbulence affect fog properties. Under polluted conditions, the higher fog top strengthens the fog-top long-wave radiative cooling and then reduces the strength of temperature inversion near the surface and enhances turbulence. Stronger turbulence further increases the fog-top height and fog area. Due to more conducive meteorological conditions, the feedbacks are stronger in Fog2 than in Fog1, contributing to enhancing AFI.

Our findings can be generalized due to the following reasons. First, the simulation design is reasonable. Similar to many previous studies, polluted and clean conditions are simulated through varying emission intensity. Second, the conclusions are robust, because they are derived from physical analyses. The interaction between aerosol loading, fog macro- and microphysical properties, and boundary layer meteorological conditions are understood physically. Third, the fog events are typical and have large coverage. Therefore, the findings in this study can be generalized, at least in polluted fog events during winter. Besides, there are large uncertainties in the aerosol–cloud interaction (Fan et al.,2016; Guo et al., 2018; Rosenfeld et al., 2019; Seinfeld et al., 2016; Zhu and Penner, 2020; Zhu et al., 2019). The findings in our article shed new light on whether mechanisms responsible for evolution of AFI are at play in aerosol–cloud interaction, particularly for stratus, which is similar to fog.

Data and code availability. The data repositories have been listed in Sect. 2. Codes can be accessed by contacting Chunsong Lu via luchunsong110@gmail.com.

Author contributions. NS performed the data analysis, model simulation, and article writing. CL proposed the idea, supervised the work, and revised the article. XJ and YW both took part in revising the article and gave suggestions. Ground-based observation data were provided by

XJ and DL. YL supervised the analysis of the turbulence kinetic energy budget. TZ supported the work that anthropogenic emissions were driven by Multiresolution Emission Inventory for China (MECI). SN provided financial support. NS prepared the article with help from YY, BZ, SF, SY, and JL.

Competing interests. The authors in this article declare that they have no conflict of interest with others.

Acknowledgements. This Article is supported by the National Key Scientific and Technological Infrastructure project "Earth System Science Numerical Simulator Facility" (EarthLab), and we acknowledge the High Performance Computing Centre of Nanjing University of Information Science & Technology for their support of this work.

Financial support. This research has been supported by the National Natural Science Foundation of China (grant nos. 42027804, 41775134, 41975181,42205072) and the Science and Technology Planning Project of Gansu Province (grant nos. 22JR5RA445).

References

Abdul-Razzak, H.: A parameterization of aerosol activation 3. Sectional representation, J. Geophys. Res., 107, https://doi.org/10.1029/2001jd000483, 2002.

Ackerman, A. S., Kirkpatrick, M. P., Stevens, D. E., and Toon, O. B.: The impact of humidity above stratiform clouds on indirect aerosol climate forcing, Nature, 432, 1014-1017, https://doi.org/10.1038/nature03174, 2004.

Barnston, A. G.: Correspondence among the Correlation, RMSE, and Heidke Forecast Verification Measures; Refinement of the Heidke Score, Weather Forecasting, 7, 699-709, https://doi.org/10.1175/1520-0434(1992)007<0699:catcra>2.0.co;2, 1992.

Boutle, I., Price, J., Kudzotsa, I., Kokkola, H., and Romakkaniemi, S.: Aerosol–fog interaction and the transition to well-mixed radiation fog, Atmos. Chem. Phys., 18, 7827-7840, https://doi.org/10.5194/acp-18-7827-2018, 2018.

Boylan, J. W. and Russell, A. G.: PM and light extinction model performance metrics, goals, and criteria for three-dimensional air quality models, Atmos. Environ., 40, 4946-4959, https://doi.org/10.1016/j.atmosenv.2005.09.087, 2006.

Chaboureau, J.-P. and Bechtold, P.: A Simple Cloud Parameterization Derived from Cloud Resolving Model Data: Diagnostic and Prognostic Applications, J. Atmos. Sci., 59, 2362-2372, https://doi.org/10.1175/1520-0469(2002)059<2362:ascpdf>2.0.co;2, 2002.

Ding, Q., Sun, J., Huang, X., Ding, A., Zou, J., Yang, X., and Fu, C.: Impacts of black carbon on the formation of advection–radiation fog during a haze pollution episode in eastern China, Atmos. Chem. Phys., 19, 7759-7774, https://doi.org/10.5194/acp-19-7759-2019, 2019.

Ducongé, L., Lac, C., Vié, B., Bergot, T., and Price, J. D.: Fog in heterogeneous environments: the relative importance of local and non-local processes on radiative-advective fog formation, Q. J. R. Meteorolog. Soc., 146, 2522-2546, https://doi.org/10.1002/qj.3783, 2020.

Fernando, H. J. S., Gultepe, I., Dorman, C., Pardyjak, E., Wang, Q., Hoch, S. W., Richter, D., Creegan, E., Gaberšek, S., Bullock, T., Hocut, C., Chang, R., Alappattu, D., Dimitrova, R., Flagg, D., Grachev, A., Krishnamurthy, R., Singh, D. K., Lozovatsky, I., Nagare, B., Sharma, A., Wagh, S., Wainwright, C., Wroblewski, M., Yamaguchi, R., Bardoel, S., Coppersmith, R. S., Chisholm, N., Gonzalez, E., Gunawardena, N., Hyde, O., Morrison, T., Olson, A., Perelet, A., Perrie, W., Wang, S., and Wauer, B.: C-FOG: Life of Coastal Fog, Bull. Am. Meteorol. Soc., 102, E244-E272, https://doi.org/10.1175/bams-d-19-0070.1, 2021.

Fitzjarrald, D. R. and Lala, G. G.: Hudson Valley Fog Environments, J. Appl. Meteorol. Clim., 28, 1303-1328, https://doi.org/10.1175/1520-0450(1989)028<1303:hvfe>2.0.co;2, 1989.

Gao, M., Carmichael, G. R., Wang, Y., Saide, P. E., Yu, M., Xin, J., Liu, Z., and Wang, Z.: Modeling study of the 2010 regional haze event in the North China Plain, Atmos. Chem. Phys., 16, 1673-1691, https://doi.org/10.5194/acp-16-1673-2016, 2016.

Garrett, T. J. and Zhao, C.: Increased Arctic cloud longwave emissivity associated with pollution from mid-latitudes, Nature, 440, 787-789, https://doi.org/10.1038/nature04636, 2006.

Ghan, S., Wang, M., Zhang, S., Ferrachat, S., Gettelman, A., Griesfeller, J., Kipling, Z., Lohmann, U., Morrison, H., and Neubauer, D.: Challenges in constraining anthropogenic aerosol effects on cloud radiative forcing using present-day spatiotemporal variability, Proc. Natl. Acad. Sci. U.S.A., 113, 5804-5811, https://doi.org/10.1073/pnas.1514036113, 2016.

Grell, G. A. and Dévényi, D.: A generalized approach to parameterizing convection combining ensemble and data assimilation techniques, Geophys. Res. Lett., 29, 38-31-38-34, https://doi.org/10.1029/2002gl015311, 2002.

Gultepe, I., Kuhn, T., Pavolonis, M., Calvert, C., Gurka, J., Heymsfield, A. J., Liu, P. S. K., Zhou, B., Ware, R., Ferrier, B., Milbrandt, J., and Bernstein, B.: Ice Fog in Arctic During FRAM–Ice Fog Project: Aviation and Nowcasting Applications, Bull. Am. Meteorol. Soc., 95, 211-226, https://doi.org/10.1175/bams-d-11-00071.1, 2014.

Guo, L., Guo, X., Fang, C., and Zhu, S.: Observation analysis on characteristics of formation, evolution and transition of a long-lasting severe fog and haze episode in North China, Sci. China, Ser. D Earth Sci., 58, 329-344, https://doi.org/10.1007/s11430-014-4924-2, 2015.

Guo, L., Guo, X., Luan, T., Zhu, S., and Lyu, K.: Radiative effects of clouds and fog on long-lasting heavy fog events in northern China, Atmos. Res., 252, 105444, https://doi.org/10.1016/j.atmosres.2020.105444, 2021.

Haeffelin, M., Bergot, T., Elias, T., Tardif, R., Carrer, D., Chazette, P., Colomb, M., Drobinski, P., Dupont, E., Dupont, J.-C., Gomes, L., Musson-Genon, L., Pietras, C., Plana-Fattori, A., Protat, A., Rangognio, J., Raut, J.-C., Rémy, S., Richard, D., Sciare, J., and Zhang, X.: Parisfog: Shedding new Light on Fog Physical Processes, Bull. Am. Meteorol. Soc., 91, 767-783, https://doi.org/10.1175/2009bams2671.1, 2010.

Hammer, E., Gysel, M., Roberts, G. C., Elias, T., Hofer, J., Hoyle, C. R., Bukowiecki, N., Dupont, J. C., Burnet, F., Baltensperger, U., and Weingartner, E.: Size-dependent particle activation properties in fog during the ParisFog 2012/13 field campaign, Atmos. Chem. Phys., 14, 10517-10533, https://doi.org/10.5194/acp-14-10517-2014, 2014.

Holets, S. and Swanson, R. N.: High-Inversion Fog Episodes in Central California, J. Appl. Meteorol. Clim., 20, 890-899, https://doi.org/10.1175/1520-0450(1981)020<0890:hifeic>2.0.co;2, 1981.

Hu, W., Zhao, T., Bai, Y., Kong, S., Xiong, J., Sun, X., Yang, Q., Gu, Y., and Lu, H.: Importance of regional PM2.5 transport and precipitation washout in heavy air pollution in the Twain-Hu Basin over Central China: Observational analysis and WRF-Chem simulation, Sci. Total Environ., 758, 143710, https://doi.org/10.1016/j.scitotenv.2020.143710, 2021.

Iacono, M. J., Delamere, J. S., Mlawer, E. J., Shephard, M. W., Clough, S. A., and Collins, W. D.: Radiative forcing by long-lived greenhouse gases: Calculations with the AER radiative transfer models, J. Geophys. Res., 113, https://doi.org/10.1029/2008jd009944, 2008.

Jia, X., Quan, J., Zheng, Z., Liu, X., Liu, Q., He, H., and Liu, Y.: Impacts of Anthropogenic Aerosols on Fog in North China Plain, J. Geophys. Res.: Atmos., 124, 252-265, https://doi.org/10.1029/2018jd029437, 2019.

Kim, C. K. and Yum, S. S.: Local meteorological and synoptic characteristics of fogs formed over Incheon international airport in the west coast of Korea, Adv. Atmos. Sci., 27, 761-776, https://doi.org/10.1007/s00376-009-9090-7, 2010.

Kim, C. K. and Yum, S. S.: A numerical study of sea-fog formation over cold sea surface using a one-dimensional turbulence model coupled with the weather research and forecasting model, Boundary Layer Meteorol., 143, 481-505, https://doi.org/10.1007/s10546-012-9706-9, 2012.

Kim, C. K. and Yum, S. S.: A study on the transition mechanism of a stratus cloud into a warm sea fog using a single column model PAFOG coupled with WRF, Asia-Pac. J. Atmos. Sci., 49, 245-257, https://doi.org/10.1007/s13143-013-0024-z, 2013.

Kumar, B., Bera, S., Prabha, T. V., and Grabowski, W. W.: Cloud-edge mixing: Direct numerical simulation and observations in Indian Monsoon clouds, J. Adv. Model. Earth Syst., 9, 332-353, https://doi.org/10.1002/2016ms000731, 2017.

Kumar, B., Ranjan, R., Yau, M.-K., Bera, S., and Rao, S. A.: Impact of high- and low-vorticity turbulence on cloud–environment mixing and cloud microphysics processes, Atmos. Chem. Phys., 21, 12317-12329, https://doi.org/10.5194/acp-21-12317-2021, 2021.

Lee, H.-H., Chen, S.-H., Kleeman, M. J., Zhang, H., DeNero, S. P., and Joe, D. K.: Implementation of warm-cloud processes in a source-oriented WRF/Chem model to study the effect of aerosol mixing state on fog formation in the Central Valley of California, Atmos. Chem. Phys., 16, 8353-8374, https://doi.org/10.5194/acp-16-8353-2016, 2016.

Li, M., Liu, H., Geng, G., Hong, C., Liu, F., Song, Y., Tong, D., Zheng, B., Cui, H., Man, H., Zhang, Q., and He, K.: Anthropogenic emission inventories in China: a review, Natl. Sci. Rev., 4, 834-866, https://doi.org/10.1093/nsr/nwx150, 2017a.

Li, Z., Guo, J., Ding, A., Liao, H., Liu, J., Sun, Y., Wang, T., Xue, H., Zhang, H., and Zhu, B.: Aerosol and boundary-layer interactions and impact on air quality, Natl. Sci. Rev., 4, 810-833, https://doi.org/10.1093/nsr/nwx117, 2017b.

Liu, D. Y., Niu, S. J., Yang, J., Zhao, L. J., Lü, J. J., and Lu, C. S.: Summary of a 4-Year Fog Field Study in Northern Nanjing, Part 1: Fog Boundary Layer, Pure Appl. Geophys., 169, 809-819, https://doi.org/10.1007/s00024-011-0343-x, 2011.

Liu, Y., Hua, S., Jia, R., and Huang, J.: Effect of Aerosols on the Ice Cloud Properties Over the Tibetan Plateau, J. Geophys. Res.: Atmos., 124, 9594-9608, https://doi.org/10.1029/2019jd030463, 2019.

Liu, Y., Zhu, Q., Hua, S., Alam, K., Dai, T., and Cheng, Y.: Tibetan Plateau driven impact of Taklimakan dust on northern rainfall, Atmos. Environ., 234, 117583, https://doi.org/10.1016/j.atmosenv.2020.117583, 2020.

Maalick, Z., Kühn, T., Korhonen, H., Kokkola, H., Laaksonen, A., and Romakkaniemi, S.: Effect of aerosol concentration and absorbing aerosol on the radiation fog life cycle, Atmos. Environ., 133, 26-33, https://doi.org/10.1016/j.atmosenv.2016.03.018, 2016.

Maronga, B. and Bosveld, F. C.: Key parameters for the life cycle of nocturnal radiation fog: a comprehensive large-eddy simulation study, Q. J. R. Meteorolog. Soc., 143, 2463-2480, https://doi.org/10.1002/qj.3100, 2017.

Matsui, T., Zhang, S. Q., Lang, S. E., Tao, W.-K., Ichoku, C., and Peters-Lidard, C. D.: Impact of radiation frequency, precipitation radiative forcing, and radiation column aggregation on convection-permitting West African monsoon simulations, Clim. Dyn., 55, 193-213, https://doi.org/10.1007/s00382-018-4187-2, 2020.

Mazoyer, M., Burnet, F., and Denjean, C.: Experimental study on the evolution of droplet size distribution during the fog life cycle, Atmos. Chem. Phys., 22, 11305-11321, https://doi.org/10.5194/acp-22-11305-2022, 2022.

Mazoyer, M., Lac, C., Thouron, O., Bergot, T., Masson, V., and Musson-Genon, L.: Large eddy simulation of radiation fog: impact of dynamics on the fog life cycle, Atmos. Chem. Phys., 17, 13017-13035, https://doi.org/10.5194/acp-17-13017-2017, 2017.

Mazoyer, M., Burnet, F., Denjean, C., Roberts, G. C., Haeffelin, M., Dupont, J.-C., and Elias, T.: Experimental study of the aerosol impact on fog microphysics, Atmos. Chem. Phys., 19, 4323-4344, https://doi.org/10.5194/acp-19-4323-2019, 2019.

Mecikalski, J. R., Bedka, K. M., Paech, S. J., and Litten, L. A.: A Statistical Evaluation of GOES Cloud-Top Properties for Nowcasting Convective Initiation, Mon. Weather Rev., 136, 4899-4914, https://doi.org/10.1175/2008mwr2352.1, 2008.

Morrison, H., Curry, J., and Khvorostyanov, V.: A new double-moment microphysics parameterization for application in cloud and climate models. Part I: Description, J. Atmos. Sci., 62, 1665-1677, https://doi.org/10.1175/JAS3446.1, 2005.

Nakanishi, M. and Niino, H.: Development of an Improved Turbulence Closure Model for the Atmospheric Boundary Layer, J. Meteorolog. Soc. Jpn., 87, 895-912, https://doi.org/10.2151/jmsj.87.895, 2009.

Niu, S., Lu, C., Yu, H., Zhao, L., and Lü, J.: Fog research in China: An overview, Adv. Atmos. Sci., 27, 639-662, https://doi.org/10.1007/s00376-009-8174-8, 2010.

Niu, S. J., Liu, D. Y., Zhao, L. J., Lu, C. S., Lü, J. J., and Yang, J.: Summary of a 4-Year Fog Field Study in Northern Nanjing, Part 2: Fog Microphysics, Pure Appl. Geophys., 169, 1137-1155, https://doi.org/10.1007/s00024-011-0344-9, 2011.

Petters, M. D. and Kreidenweis, S. M.: A single parameter representation of hygroscopic growth and cloud condensation nucleus activity, Atmos. Chem. Phys., 7, 1961-1971, https://doi.org/10.5194/acp-7-1961-2007, 2007.

Porson, A., Price, J., Lock, A., and Clark, P.: Radiation Fog. Part II: Large-Eddy Simulations in Very Stable Conditions, Boundary Layer Meteorol., 139, 193-224, https://doi.org/10.1007/s10546-010-9579-8, 2011.

Price, J. D., Lane, S., Boutle, I. A., Smith, D. K. E., Bergot, T., Lac, C., Duconge, L., McGregor, J., Kerr-Munslow, A., Pickering, M., and Clark, R.: LANFEX: A Field and Modeling Study to Improve Our Understanding and Forecasting of Radiation Fog, Bull. Am. Meteorol. Soc., 99, 2061-2077, https://doi.org/10.1175/bams-d-16-0299.1, 2018.

Quan, J., Zhang, Q., He, H., Liu, J., Huang, M., and Jin, H.: Analysis of the formation of fog and haze in North China Plain (NCP), Atmos. Chem. Phys., 11, 8205-8214, https://doi.org/10.5194/acp-11-8205-2011, 2011.

Quan, J., Liu, Y., Jia, X., Liu, L., Dou, Y., Xin, J., and Seinfeld, J. H.: Anthropogenic aerosols prolong fog lifetime in China, Environ. Res. Lett., 16, 044048, https://doi.org/10.1088/1748-9326/abef32, 2021.

Roach, W., Brown, R., Caughey, S., Garland, J., and Readings, C.: The physics of radiation fog: I–a field study, Q. J. R. Meteorolog. Soc., 102, 313-333, https://doi.org/10.1002/qj.49710243204, 1976.

Shen, C., Zhao, C., Ma, N., Tao, J., Zhao, G., Yu, Y., and Kuang, Y.: Method to Estimate Water Vapor Supersaturation in the Ambient Activation Process Using Aerosol and Droplet Measurement Data, J. Geophys. Res.: Atmos., 123, https://doi.org/10.1029/2018jd028315, 2018.

Simmel, M. and Wurzler, S.: Condensation and activation in sectional cloud microphysical models, Atmos. Res., 80, 218-236, https://doi.org/10.1016/j.atmosres.2005.08.002, 2006.

Steeneveld, G. J. and de Bode, M.: Unravelling the relative roles of physical processes in modelling the life cycle of a warm radiation fog, Q. J. R. Meteorolog. Soc., 144, 1539-1554, https://doi.org/10.1002/qj.3300, 2018.

Stolaki, S., Haeffelin, M., Lac, C., Dupont, J. C., Elias, T., and Masson, V.: Influence of aerosols on the life cycle of a radiation fog event. A numerical and observational study, Atmos. Res., 151, 146-161, https://doi.org/10.1016/j.atmosres.2014.04.013, 2015.

Toll, V., Christensen, M., Quaas, J., and Bellouin, N.: Weak average liquid-cloud-water response to anthropogenic aerosols, Nature, 572, 51-55, https://doi.org/10.1038/s41586-019-1423-9, 2019.

Twomey, S.: The influence of pollution on the shortwave albedo of clouds, J. Atmos. Sci., 34, 1149-1152, https://doi.org/10.1175/1520-0469(1977)034<1149:TIOPOT>2.0.CO;2, 1977.

Vautard, R., Yiou, P., and van Oldenborgh, G. J.: Decline of fog, mist and haze in Europe over the past 30 years, Nat. Geosci., 2, 115-119, https://doi.org/10.1038/ngeo414, 2009.
Wærsted, E. G., Haeffelin, M., Dupont, J.-C., Delanoë, J., and Dubuisson, P.: Radiation in fog: quantification of the impact on fog liquid water based on ground-based remote sensing, Atmos. Chem. Phys., 17, 10811-10835, https://doi.org/10.5194/acp-17-10811-2017, 2017.
Wang, Y., Fan, J., Zhang, R., Leung, L. R., and Franklin, C.: Improving bulk microphysics parameterizations in simulations of aerosol effects, J. Geophys. Res.: Atmos., 118, 5361-5379, https://doi.org/10.1002/jgrd.50432, 2013.
Wang, Y., Lu, C., Niu, S., Lv, J., Jia, X., Xu, X., Xue, Y., Zhu, L., and Yan, S.: Diverse dispersion effects and parameterization of relative dispersion in urban fog in eastern China, J. Geophys. Res.: Atmos., n/a, e2022JD037514, https://doi.org/10.1029/2022JD037514, 2023.
Wang, Y., Vogel, J. M., Lin, Y., Pan, B., Hu, J., Liu, Y., Dong, X., Jiang, J. H., Yung, Y. L., and Zhang, R.: Aerosol microphysical and radiative effects on continental cloud ensembles, Adv. Atmos. Sci., 35, 234-247, https://doi.org/10.1007/s00376-017-7091-5, 2018.
Wang, Y., Niu, S., Lu, C., Lv, J., Zhang, J., Zhang, H., Zhang, S., Shao, N., Sun, W., Jin, Y., and Song, Q.: Observational study of the physical and chemical characteristics of the winter radiation fog in the tropical rainforest in Xishuangbanna, China, Sci. China, Ser. D Earth Sci., 64, 1982-1995, https://doi.org/10.1007/s11430-020-9766-4, 2021.
WMO: International meteorological vocabulary, WMO-182, 784 pp., 1992.
Xu, X., Lu, C., Liu, Y., Gao, W., Wang, Y., Cheng, Y., Luo, S., and Van Weverberg, K.: Effects of Cloud Liquid-Phase Microphysical Processes in Mixed-Phase Cumuli Over the Tibetan Plateau, J. Geophys. Res.: Atmos., 125, https://doi.org/10.1029/2020jd033371, 2020.
Yamane, Y., Hayashi, T., Dewan, A. M., and Akter, F.: Severe local convective storms in Bangladesh: Part II, Atmos. Res., 95, 407-418, https://doi.org/10.1016/j.atmosres.2009.11.003, 2010.

Yan, S., Zhu, B., Huang, Y., Zhu, J., Kang, H., Lu, C., and Zhu, T.: To what extents do urbanization and air pollution affect fog?, Atmos. Chem. Phys., 20, 5559-5572, https://doi.org/10.5194/acp-20-5559-2020, 2020.

Yan, S., Zhu, B., Zhu, T., Shi, C., Liu, D., Kang, H., Lu, W., and Lu, C.: The Effect of Aerosols on Fog Lifetime: Observational Evidence and Model Simulations, Geophys. Res. Lett., 48, https://doi.org/10.1029/2020gl091156, 2021.

Yang, Q., Zhao, T., Tian, Z., Kumar, K. R., Chang, J., Hu, W., Shu, Z., and Hu, J.: The Cross-Border Transport of PM2.5 from the Southeast Asian Biomass Burning Emissions and Its Impact on Air Pollution in Yunnan Plateau, Southwest China, Remote Sens., 14, 1886, https://doi.org/10.3390/rs14081886, 2022.

Yang, Y., Hu, X.-M., Gao, S., and Wang, Y.: Sensitivity of WRF simulations with the YSU PBL scheme to the lowest model level height for a sea fog event over the Yellow Sea, Atmos. Res., 215, 253-267, https://doi.org/10.1016/j.atmosres.2018.09.004, 2019.

Ye, X., Wu, B., and Zhang, H.: The turbulent structure and transport in fog layers observed over the Tianjin area, Atmos. Res., 153, 217-234, https://doi.org/10.1016/j.atmosres.2014.08.003, 2015.

Yum, S. S. and Hudson, J. G.: Adiabatic predictions and observations of cloud droplet spectral broadness, Atmos. Res., 73, 203-223, https://doi.org/10.1016/j.atmosres.2004.10.006, 2005.

Zaveri, R. A. and Peters, L. K.: A new lumped structure photochemical mechanism for large-scale applications, J. Geophys. Res.: Atmos., 104, 30387-30415, https://doi.org/10.1029/1999jd900876, 1999.

Zaveri, R. A., Easter, R. C., Fast, J. D., and Peters, L. K.: Model for Simulating Aerosol Interactions and Chemistry (MOSAIC), J. Geophys. Res., 113, https://doi.org/10.1029/2007jd008782, 2008.

Zhao, C. and Garrett, T. J.: Effects of Arctic haze on surface cloud radiative forcing, Geophys. Res. Lett., 42, 557-564, https://doi.org/10.1002/2014gl062015, 2015.

Zhao, L., Niu, S., Zhang, Y., and Xu, F.: Microphysical characteristics of sea fog over the east coast of Leizhou Peninsula, China, Adv. Atmos. Sci., 30, 1154-1172, https://doi.org/10.1007/s00376-012-1266-x, 2013.

Zheng, B., Tong, D., Li, M., Liu, F., Hong, C., Geng, G., Li, H., Li, X., Peng, L., Qi, J., Yan, L., Zhang, Y., Zhao, H., Zheng, Y., He, K., and Zhang, Q.: Trends in China's anthropogenic emissions since 2010 as the consequence of clean air actions, Atmos. Chem. Phys., 18, 14095-14111, https://doi.org/10.5194/acp-18-14095-2018, 2018.

Zhong, J., Zhang, X., Wang, Y., Liu, C., and Dong, Y.: Heavy aerosol pollution episodes in winter Beijing enhanced by radiative cooling effects of aerosols, Atmos. Res., 209, 59-64, https://doi.org/10.1016/j.atmosres.2018.03.011, 2018.

Zhou, B. and Ferrier, B. S.: Asymptotic Analysis of Equilibrium in Radiation Fog, J. Appl. Meteorol. Clim., 47, 1704-1722, https://doi.org/10.1175/2007jamc1685.1, 2008.

Zhu, J., Zhu, B., Huang, Y., An, J., and Xu, J.: PM2.5 vertical variation during a fog episode in a rural area of the Yangtze River Delta, China, Sci. Total Environ., 685, 555-563, https://doi.org/10.1016/j.scitotenv.2019.05.319, 2019.

Table 1. Summary of major parameterisation schemes.

Scheme	Option
Microphysics	Morrison
Boundary layer	MYNN
Shortwave radiation	Goddard
Longwave radiation	RRTMG
Cumulus	Grell 3D
Aerosol chemistry	MOSAIC (4 bins)
Gas phase chemistry	CBMZ

Table 2. Evaluation of $PM_{2.5}$ mass concentration. NMB, NME, MFB, and MFE stand for normalised mean bias, normalised mean error, mean fractional bias, and mean fractional error, respectively. Time '2514' (DateHour) indicates 14:00 local standard time (LST) (LST = Universal Time Coordinated + 8 h) on 25 November 2018. The other time expressions follow the same logic.

DateHour	NMB(%)	NME(%)	MFB(%)	MFE(%)
2514-2614	13	25	13	24
2614-2714	38	42	35	38
Total	25	30	24	28

Table 3. The elements a-d in the Heidke Skill Score calculation

	Observed fog	No fog observed
Fog simulated	a	b
No fog simulated	c	d

Table 4. Quantitative estimation of AFI strength in two fog events (Fog1 and Fog2), including the responses of fog optical depth (FOD), liquid water path (LWP), and fog effective radius (R_e) to the changes in fog droplet number concentration (N_f). The EXP1 is that two fog events are both under polluted conditions, and EXP2 is under clean conditions. The EXP3 is that Fog1 is under clean conditions and Fog2 is under polluted conditions. The ratio is the relative change between Fog1 and Fog2, calculated as (Fog2 − Fog1)/Fog1. In the fourth and sixth columns, Fog1 in both EXP2 and EXP3 is under clean conditions.

	EXP1 vs EXP2			EXP3 vs EXP2		
	Fog1	Fog2	Ratio	Fog1	Fog2	Ratio
$\Delta\ln FOD/\Delta\ln N_f$	0.98	1.32	34.7%	–	1.17	–
$\Delta\ln LWP/\Delta\ln N_f$	0.76	1.08	42.1%	–	1.00	–
$-\Delta\ln R_e/\Delta\ln N_f$	0.22	0.24	9.1%	–	0.17	–

Table 5. Average 2 m relative humidity (RH_{2m}) and planetary boundary layer height (PBLH) above the ground in domain 03 during 12:00–20:00 local standard time (LST) (LST = Universal Time Coordinated + 8 h) on 25 and 26 November 2018 under clean and polluted conditions. DIF is the difference in each property between 25 and 26 November.

	Clean			Polluted		
	Nov. 25th	Nov. 26th	DIF	Nov. 25th	Nov. 26th	DIF
RH_{2m} (%)	76	80	4	76	82	6
PBLH (m)	669	610	-59	670	578	-92

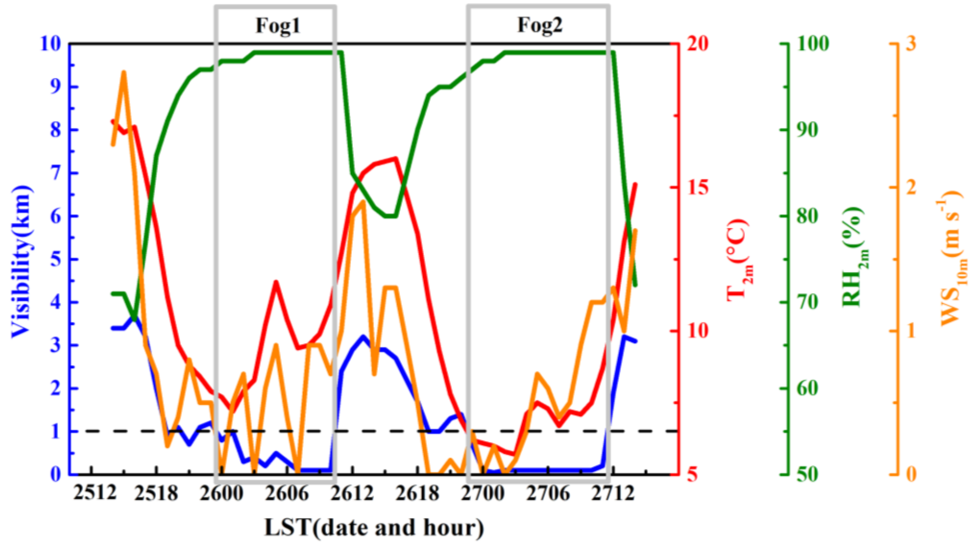

Figure 1. Time series of visibility, 2 m temperature (T_{2m}), 2 m relative humidity (RH_{2m}), and 10 m wind speed (WS_{10m}) above the ground at the Nanjing observation site (31.93°N, 118.9°E). Fog1 and Fog2 in the light grey box are the two fog events. Time '2512' indicates 12:00 local standard time (LST) (LST = Universal Time Coordinated + 8 h) on 25 November 2018. The other time expressions follow the same logic.

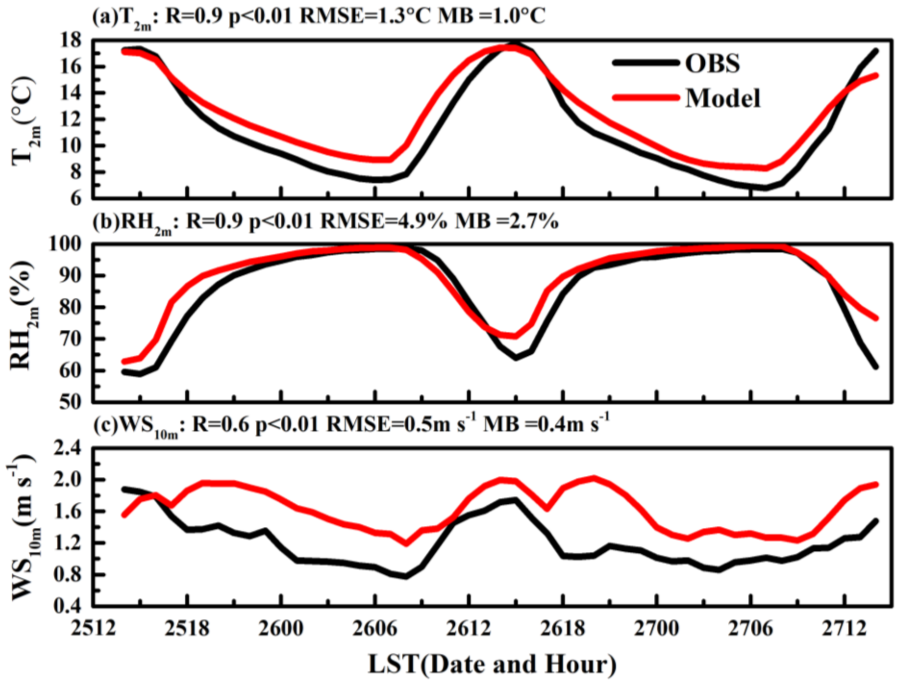

Figure 2. Hourly variations in observed (black lines) and simulated (red lines) meteorological properties, including (a) 2 m temperature (T_{2m}), (b) 2 m relative humidity (RH_{2m}), and (c) 10 m wind speed (WS_{10m}) above the ground, averaged over 104 meteorological stations in domain 03 from 14:00 local standard time (LST) (LST = Universal Time Coordinated + 8 h) on 25 November to 14:00 LST on 27 November 2018. R, p, RMSE, and MB indicate the correlation coefficient, significance level, root-mean-square error, and mean bias, respectively. Time ‘2512’ indicates 12:00 LST on 25 November 2018. The other time expressions follow the same logic.

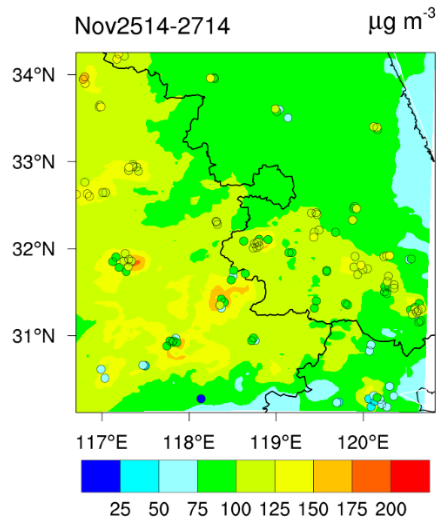

Figure 3. Simulated (shaded area) and observed (coloured dots) average distributions of $PM_{2.5}$ concentration (μg m^{-3}) from 14:00 local standard time (LST) (LST = Universal Time Coordinated + 8 h) on 25 November to 14:00 LST on 27 November 2018.

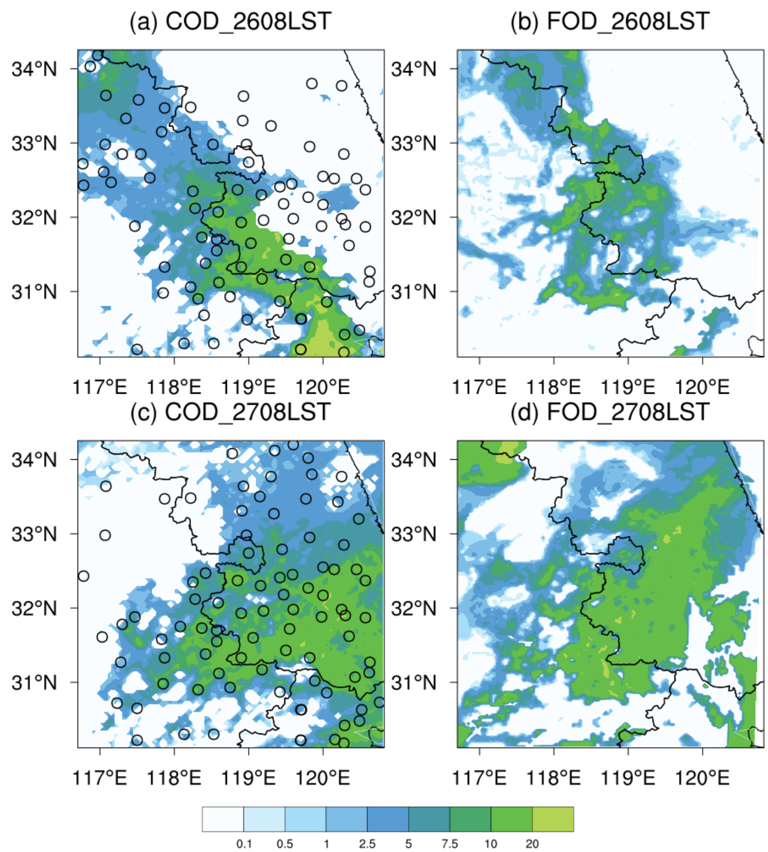

Figure 4. (a, c) Distributions of ground-based fog observations (the circular points) and cloud optical depth from Himawari-8 products at 08:00 LST on 26-27 November 2018. (b, d) Simulated fog optical depth (FOD) distributions in the domain 03 at the corresponding time of observations. Time ‘2608LST’ indicates 08:00 local standard time (LST) (LST = Universal Time Coordinated + 8 h) on 26 November 2018. The other time expressions follow the same logic.

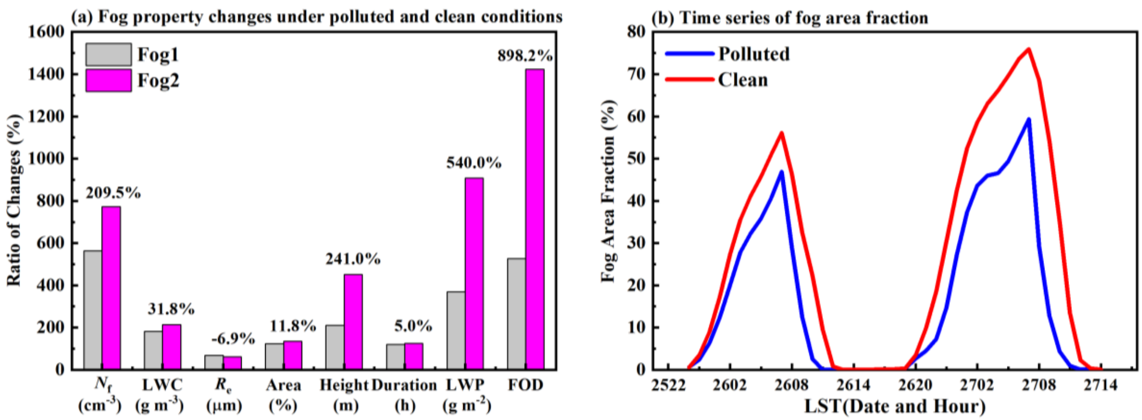

Figure 5. (a) Aerosol-induced changes in macro- and microphysical properties during the first fog (Fog1) and the second fog (Fog2) under polluted and clean conditions. (b) Temporal evolution of fog area fraction under clean and polluted conditions. N_f, LWC, R_e, Area, Height, Duration, LWP, and FOD indicate fog droplet number concentration, liquid water content, effective radius, fog area fraction, fog-top height, liquid water path, and fog optical depth, respectively. The ratios of changes are calculated by Polluted/Clean in Fig. 5a which reveal the aerosol-induced changes. The numbers above the bars in Fig. 5a represent the difference in those ratios of changes between Fog1 and Fog2 (calculated by Fog2-Fog1). Time ‘2522’ in Fig. 5b indicates 22:00 local standard time (LST) (LST = Universal Time Coordinated + 8 h) on 25 November 2018. The other time expressions follow the same logic.

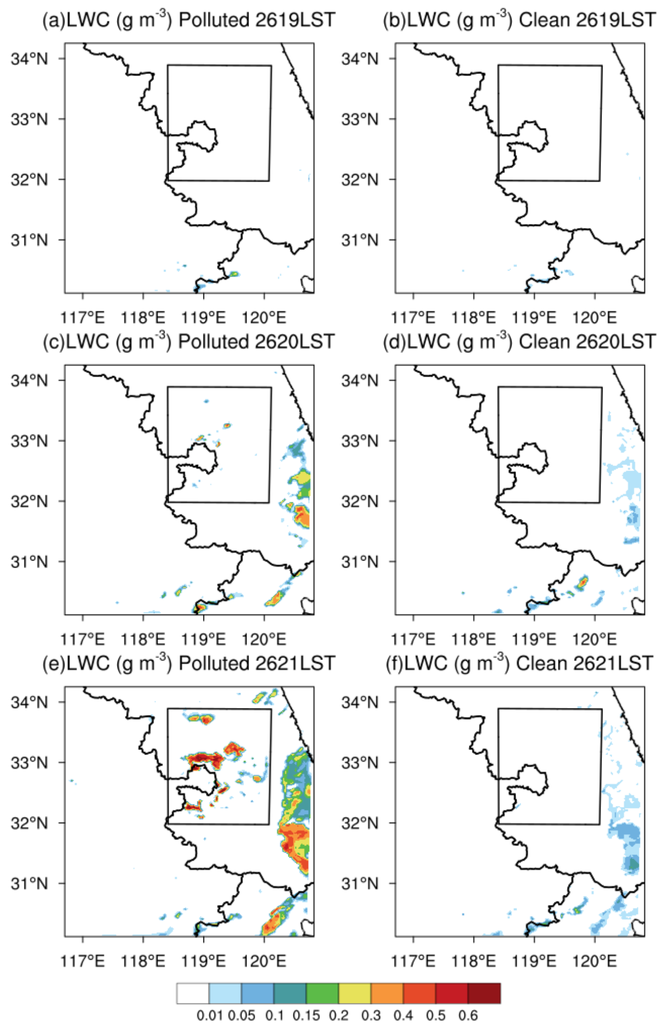

Figure 6. Liquid water content (LWC) distribution at the bottom layer from 19:00-21:00 local standard time (LST) (LST = Universal Time Coordinated + 8 h) on 26 November 2018 under (a, c, e) polluted and (b, d, f) clean conditions. The black box is the area in which Fog2 formed earlier under polluted condition. Time '2619LST' indicates 19:00 LST on 26 November 2018. The other time expressions follow the same logic.

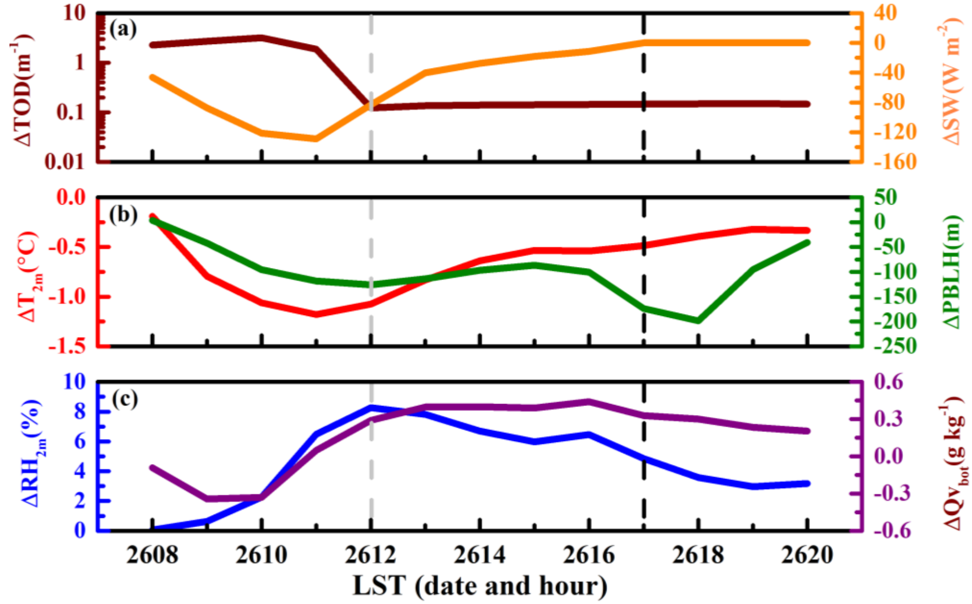

Figure 7. Differences in properties between polluted and clean conditions in the black box in Fig. 6, including (a) total optical depth (TOD), surface downwelling shortwave radiation (SW), (b) 2 m temperature (T_{2m}), planetary boundary layer height (PBLH), (c) 2 m relative humidity (RH_{2m}), and water vapour mixing ratio at the bottom of the model (Qv_{bot}), where TOD = FOD (fog optical depth) + AOD (aerosol optical path). Grey dashed line is the time of complete evaporation of Fog1 under polluted conditions. Black dashed line is the time of sunset. Time '2608' indicates 08:00 local standard time (LST) (LST = Universal Time Coordinated + 8 h) on 26 November 2018. The other time expressions follow the same logic.

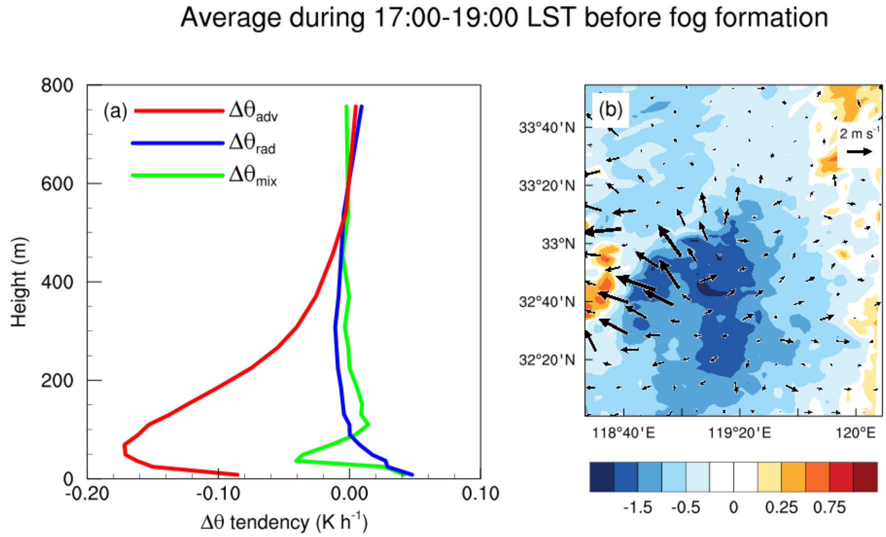

Figure 8. (a) Differences (Polluted − Clean) in terms contributing to the potential temperature tendency, including radiation (θ_{rad}), vertical mixing (θ_{mix}), and advection (θ_{adv}) in the black box in Fig. 6 before fog formation (17:00–19:00 local standard time [LST = Universal Time Coordinated + 8 h]). (b) The shaded area is the mean temperature difference (Polluted − Clean), and vectors are the mean wind vector difference (Polluted − Clean) at the bottom of the model.

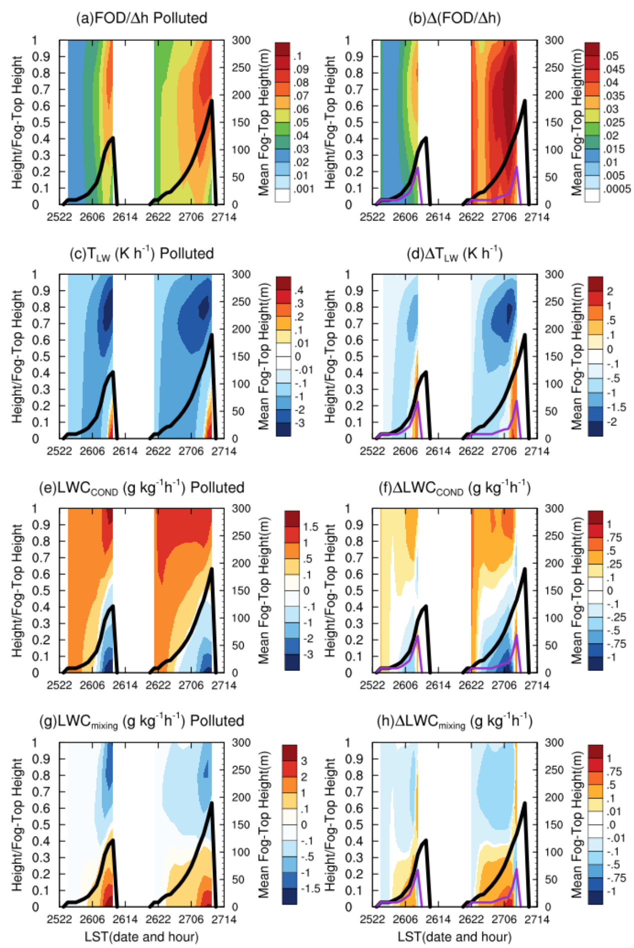

Figure 9. Time-height profiles of (a-b) average extinction coefficient through the fog layers, which is fog optical depth (FOD) at per unit height (FOD/Δh), (c-d) radiative cooling rate (T_{LW}), (e-f) condensation growth rate (LWC_{COND}), and (g-h) liquid water content tendency due to vertical mixing (LWC_{mixing}). Heights on the left axes are normalised by the fog-top heights and the left axes are mean fog-top heights. The left column is polluted conditions and the right one is the difference (Polluted − Clean). Black and purple lines are the mean fog top heights under polluted and clean conditions, respectively. Time '2522' indicates 22:00 local standard time (LST) (LST = Universal Time Coordinated + 8 h) on 25 November 2018. The other time expressions follow the same logic.

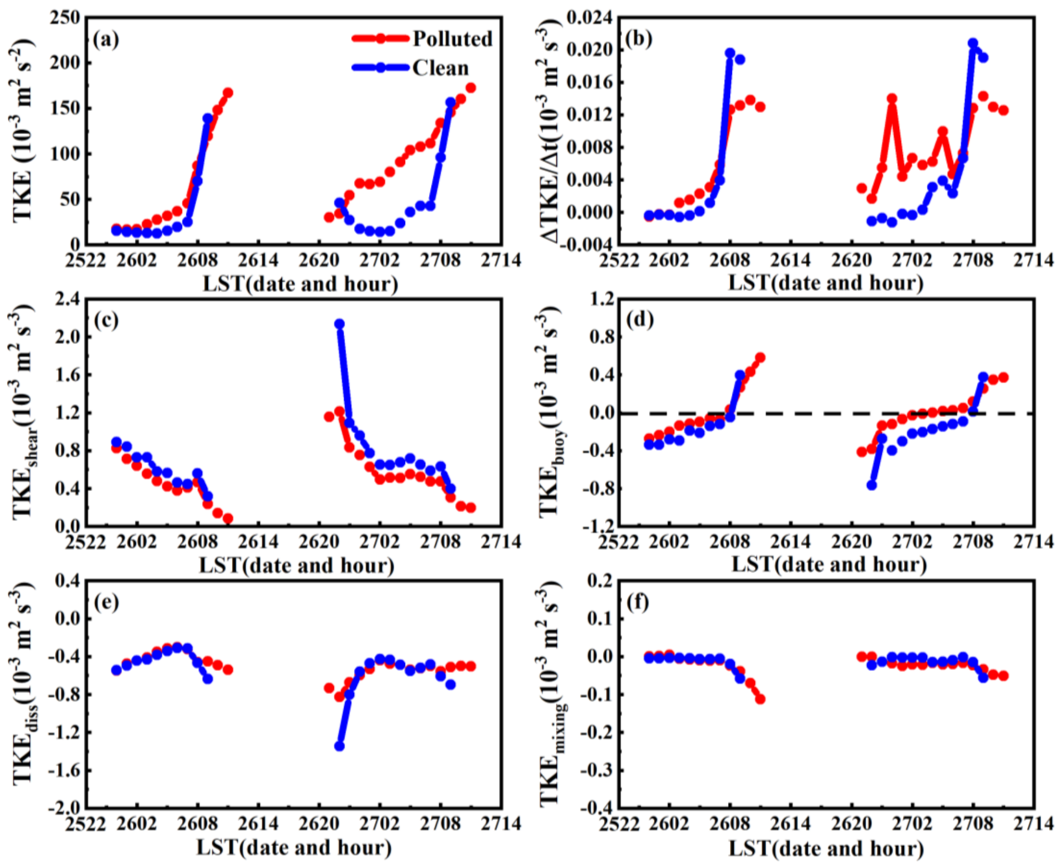

Figure 10. (a) Temporal evolution of turbulent kinetic energy (TKE), (b) TKE tendency, (c) wind shear term (TKE_{shear}), (d) buoyancy term (TKE_{buoy}), (e) dissipation term (TKE_{diss}), and (f) vertical mixing terms (TKE_{mixing}) under polluted and clean conditions. Dashed line is the zero line for TKE_{buoy}. Time '2522' indicates 22:00 local standard time (LST) (LST = Universal Time Coordinated + 8 h) on 25 November 2018. The other time expressions follow the same logic.

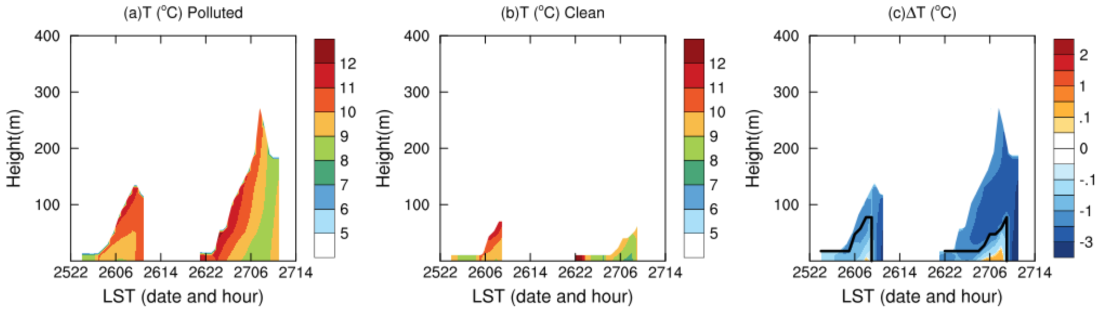

Figure 11. Time-height profiles of in-fog temperature (T) under (a) polluted and (b) clean conditions. (c) Difference between polluted and clean conditions. Black line on the right side is the maximal fog-top height under clean conditions. Time ‘2522’ indicates 22:00 local standard time (LST) (LST = Universal Time Coordinated + 8 h) on 25 November 2018. The other time expressions follow the same logic.

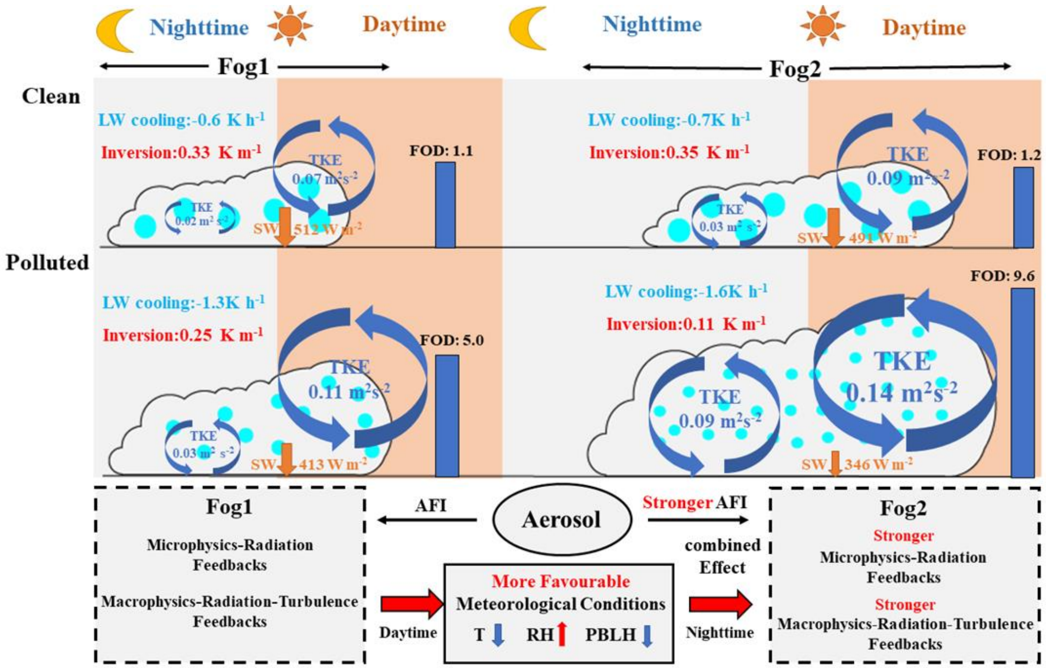

Figure 12. Conceptual image of interactions between aerosol–fog interaction (AFI) and planetary boundary layer (PBL). FOD, SW, LW, TKE, T, RH, and PBLH stand for fog optical depth, short-wave radiation, long-wave radiation, turbulent kinetic energy, temperature, relative humidity, and planetary boundary layer height, respectively. LW and inversion are at night time, and FOD is at daytime.